Evaluating post-perovskite as a cause of D″ anisotropy in regions of palaeosubduction

Andy Nowacki, Andrew M. Walker, James Wookey and J.-Michael Kendall

School of Earth Sciences, University of Bristol, Wills Memorial Building, Bristol, BS8 1RJ, *UK. E-mail: andy.nowacki@bristol.ac.uk*

SUMMARY

Seismic anisotropy in the Earth's lowermost mantle (D″) is often attributed to the alignment of $MgSiO_3$ post-perovskite (ppv) by the movement of dislocations in response to mantle flow. However, ppv's plastic yield surface is not known; nor do we know if this is the main deformation mechanism. We make use of a heterogeneous, generally anisotropic model of elasticity in D″ derived from a 3-D model of mantle flow, which is obtained by inversion of geophysical observables. Unlike previous approaches, completely general, 3-D flow and full anisotropy are permitted, yielding more information to compare with observations than has been possible before. We model observations of anisotropy in D″ by calculating the shear wave splitting predicted in ScS waves for a series of models of ppv plasticity. We find that observations in regions of the lowermost mantle beneath subduction zones are best fit by a model which accommodates slip on (010). Our results show that, within one standard deviation, slip on (010)—or a mechanism giving the same style of anisotropy—explains D″ anisotropy beneath these regions.

Key words: Mantle processes; Creep and deformation; Seismic anisotropy; Dynamics of lithosphere and mantle; Rheology: mantle.

1 INTRODUCTION

Observations of seismic anisotropy in the Earth's lowermost mantle (D″ layer) are numerous (e.g. Kendall & Silver 1998; Lay *et al.* 1998; Nowacki *et al.* 2011), yet at present it is difficult to ascribe this anisotropy to any particular causative mechanism, limiting the further utility of these observations. In this study we assess one hypothesis regarding the cause of anisotropy in the lowermost mantle: that lattice-preferred orientation (LPO) in post-perovskite (ppv) is created in response to mantle motion. We do so using the least ambiguous observations of anisotropy in D″: shear wave splitting of the seismic phase ScS, which traverses the D″ region.

Recent advances in computational and experimental mineral physics are providing new insights into the elasticity and rheology of lower mantle minerals (e.g. McCormack *et al.* 2011; Shieh *et al.* 2011; Cordier *et al.* 2012; Niwa *et al.* 2012). Tomography models can now be combined with constraints from mineral physics to predict models of mantle flow (Forte & Mitrovica 2001; Simmons *et al.* 2009, 2010). Finally, the proliferation of seismic networks is providing unprecedented coverage of anisotropy in the lowermost mantle (e.g. Nowacki *et al.* 2010). A few studies have previously tried to link flow models, mineral physics and observations of seismic anisotropy in the lowermost mantle (Wenk *et al.* 2006; Merkel *et al.* 2007; Walker *et al.* 2011; Wenk *et al.* 2011). However, all previous attempts have either made the simplifying assumption that

the style of anisotropy is transversely isotropic with a vertical symmetry axis (VTI), or imposed 2-D flow, also limiting the types of anisotropy permitted. Here, for the first time, we compare seismic observations with predictions of D″ anisotropy that are based on 3-D state-of-the-art flow models with no assumptions about the style of anisotropy. In other words we allow the anisotropy to be general in form and arbitrary in orientation.

The ppv polymorph of $MgSiO_3$ (ppv) has been proposed as a potential cause for anisotropy in D″, as it exhibits stronger single-crystal anisotropy than the perovskite (pv) phase (Iitaka *et al.* 2004; Murakami *et al.* 2004; Oganov & Ono 2004; Tsuchiya *et al.* 2004; Wookey *et al.* 2005b), and pv is believed to transform into the ppv structure at depths near to the observed D″ discontinuity (Iitaka *et al.* 2004; Murakami *et al.* 2004; Oganov & Ono 2004). Attention has focussed on ppv because it is more abundant than ferropericlase ((Mg,Fe)O, fpc) in the assumed lower mantle composition, thus a weaker LPO in ppv can cause the same strength of anisotropy than for other D″ phases. Ppv may be observed through its seismic anisotropy, provided it develops a sufficient LPO, and it is deformed enough while stable within the lowermost mantle. Some convection simulations with Earth-like parameters have indeed suggested that strain rates are high enough in D″ for dislocation creep to dominate (e.g. McNamara *et al.* 2003), which would allow LPO to form.

Despite predictions of the presence of ppv in D″, so far no data have confirmed that another cause, such as LPO in another phase,

or shape-preferred orientation (SPO) of seismically distinct material above the CMB (e.g. Kendall & Silver 1996), is inadequate to explain D″ anisotropy. Hence we attempt to test ppv LPO as a candidate mechanism. Because the pv–ppv transition has a positive Clapeyron slope, it is most likely to be found in colder regions, such as where subducted slabs have most recently reached the core–mantle boundary (CMB). We, therefore, focus on observations which sample seismically fast regions, which are believed to correspond to areas of palaeosubduction.

2 METHODS AND DATA

2.1 Observations

We consider nine previous measurements of differential S–ScS shear wave splitting in D″ in regions of palaeosubduction (Lithgow-Bertelloni & Richards 1998), shown in Fig. 1. (For details of the method, see Wookey *et al.* 2005a; Nowacki *et al.* 2010). These give coverage beneath North and Central America, the northwest Pacific and Siberia. Each result is a stack of shear wave splitting measurements, incorporating several seismic stations, and in some cases more than one earthquake. All measurements correct for upper mantle (UM) seismic anisotropy beneath the station using previous measurements of SKS splitting there, assuming that any contribution to SKS splitting from the lower mantle is negligible or would be detected as periodic variation in splitting parameters with back-azimuth. Some measurements which use shallow earthquakes also correct for anisotropy in the UM near the source. The data are used because a series of rigorous tests of the quality of the measurements is applied in all cases: good signal-to-noise ratio, clear elliptical particle motion before and linear particle motion after correction with the optimum measured splitting parameters, correction for UM splitting only where SKS results show no variation with back-azimuth, and retrieved source polarization matches that predicted by the event's focal mechanism. (See Nowacki *et al.* 2010, 2012, for more details.) The main criterion beyond this, however, is that no symmetry is imposed on the style of anisotropy in making these observations.

2.2 Elasticity calculation from mantle flow

We calculate the elasticity for a wholly ppv D″ in the regions of interest on a 5°-by-5° longitude–latitude grid at several radii spaced 50 km apart, starting at a radius of 3505 km (giving 'layers' at 25, 75, 125 and 175 km above the CMB). The procedure, similar to that of of Merkel *et al.* (2007) and Wenk *et al.* (2011), is described in detail by Walker *et al.* (2011). Briefly, for each point where the elasticity is required we trace pathlines from the pv to ppv phase transition to the point through a mantle flow field derived from the joint inversion of seismological and geodynamic data (model TX2008.V2, Forte 2000; Mitrovica & Forte 2004; Simmons *et al.* 2009). We use the values of the Clapeyron slope of the pv–ppv transition given by Oganov & Ono (2004), as this relatively large value will maximize the topography of the transition. On regular time steps along the pathlines we accumulate velocity gradient tensors and use these to drive a viscoplastic self-consistent model (Lebensohn & Tomé 1993) of texture development in a sample of 500 ppv crystals. Finally, we convert the crystal orientations to an estimate of the bulk elasticity making use of the single crystal elasticity (Stackhouse *et al.* 2006; Wentzcovitch *et al.* 2006; Stackhouse & Brodholt 2008). The end result is a set of heterogeneous, generally anisotropic elastic constants where no symmetry on the style of elasticity is imposed. The three output models are named P100, P010 and P001, the three digits giving the Miller indices of the primary crystallographic plane on which slip is accommodated (Merkel *et al.* 2007; Metsue *et al.* 2009; Miyagi *et al.* 2010) in the VPSC calculation—for more details, see Walker *et al.* (2011). The elasticity, shown by strength of anisotropy, is summarized in Fig. 2. We use the universal elastic anisotropy index, $A^U = 5G^V/G^R + K^V/K^R - 6$ (Ranganathan & Ostoja-Starzewski 2008), where G is the shear modulus, K the bulk modulus and the V and R superscripts denote the Voigt and Reuss bounds on these properties respectively. It is a measure from 0 upwards of the strength of anisotropy of a set of elastic constants, but does not capture the variation in shear wave splitting along any particular orientation.

We also performed similar calculations with a mixture of ppv and MgO with ratio 80:20 per cent (supporting information), but find that the main effect of this is to reduce the strength of anisotropy without affecting the pattern.
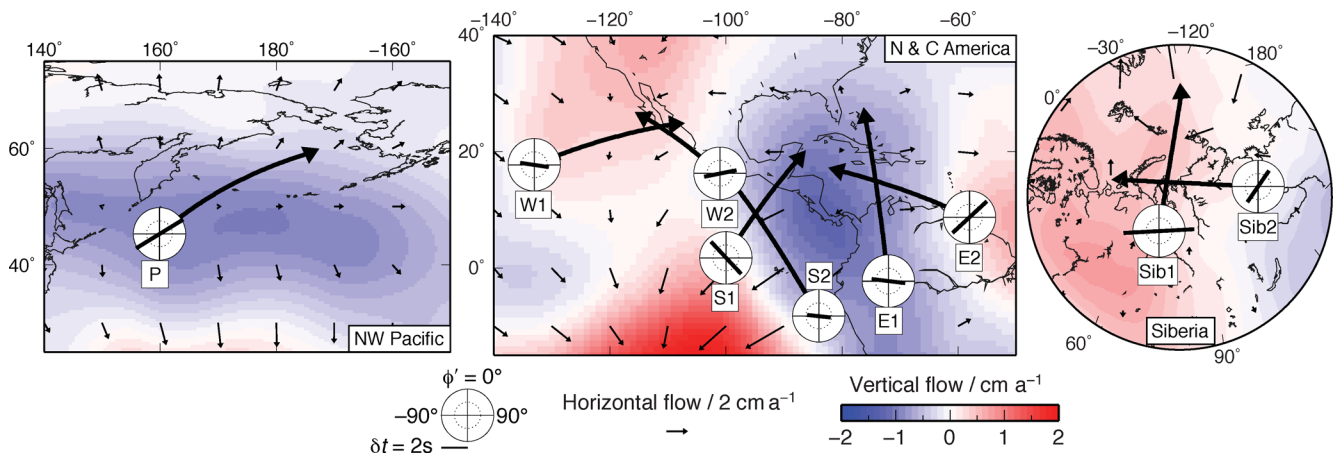
Figure 1. Previous multiazimuth observations of shear wave splitting in D″, beneath North and Central America, the northwest Pacific and Siberia. Background colour and arrows show vertical and horizontal components respectively of flow 200 km above the CMB in the TX2008 model of Simmons *et al.* (2009). Circles with bars show shear wave splitting observations in ScS phase from Nowacki *et al.* (2010) (left), Wookey *et al.* (2005a) (middle) and Wookey & Kendall (2008) (right). Orientation of bar corresponds to fast orientation in ray frame, ϕ'; length of bar corresponds to delay time, δt (see legend). Thick blacks lines are representative ray paths in the bottom 250 km of the mantle along which the splitting measurements are made; arrows show sense of direction.
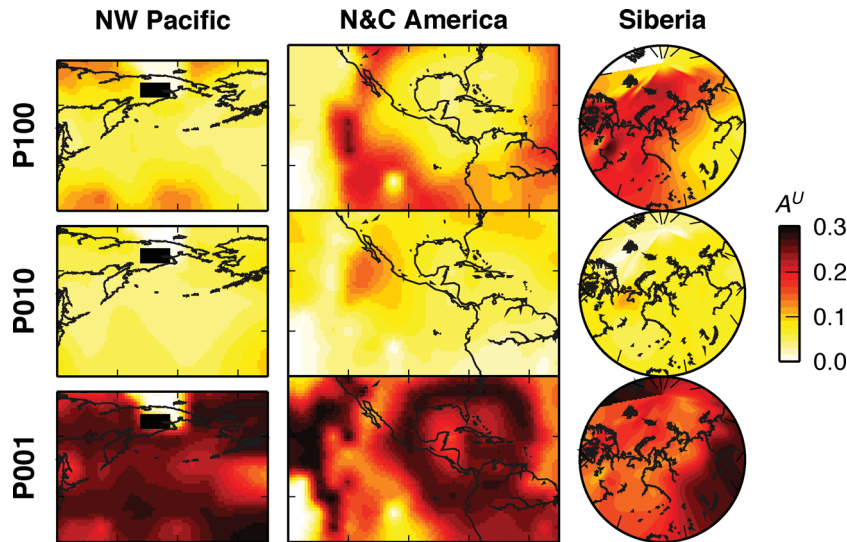
Figure 2. Strength of anisotropy of elastic constants in D″ calculated at a radius of 3505 km (25 km above the CMB), shown with the universal elastic anisotropy index, A^U. The values for each of the plasticity models (P100, P010 and P001) are given for each of the three regions. Darker colours indicate stronger anisotropy. Black squares in NW Pacific region show points where pv and not ppv is not stable at this radius (temperature and pressure) for our Clapeyron slope, and where we therefore assume isotropy.

2.3 Shear wave splitting calculation

Rays are traced through the 1-D Earth model AK135 (Kennett *et al.* 1995) along the great circle paths of the observations, and followed from their entry into the anisotropic region. While in the anisotropic region, they are repeatedly propagated forward along their 1-D ray paths by a small increment, δs. At each step, i, the local elastic constants and the ray's orientation are used to calculate the shear wave splitting for that step, $\Gamma_i = (\phi_i', \delta t_i)$. The elastic constants from the texture calculation are regridded onto a 50-km cartesian grid of nodes which determine the local elasticity at each calculation point. Provided δs is less than ∼10 per cent of the node spacing, we find no reduction in the total amount of splitting due to incomplete traversal of cells. Here, we use a value of 1 km for δs.

The splitting at each step is used as the input for the subsequent procedure. A synthetic waveform is created with the source polarization predicted by the Global CMT solution for the event used in the observation. In some cases more than one event is used in a stacked measurement, in which case a representative polarization is used; however, events for one path typically share a common tectonic mechanism, so the source polarizations do not vary much. In any case, tests showed varying the source polarization had very little effect on the results. White noise is added to the trace with amplitude 0.1 of the signal to stabilize the splitting analysis.

The synthetic waveform is then split in turn by each local value of Γ_i. This is done in the frequency domain to reduce numerical noise and avoid the necessity of using very small sampling intervals, which would increase the computational cost. Tests showed the shape of the waveform has no effect on the predicted splitting. A waveform of period 100 s is used, because along some paths the total amount of splitting is very large. This violates the assumption of the minimum eigenvalue (Silver & Chan 1991) shear wave splitting measurement technique, which is that δt is somewhat less than the period of the wave. In practice, we retrieve similar results using a wave of period 10 s, but the uncertainties are larger, hence we retain the long-period results for further study.

We then analyse the split waves using the minimum-eigenvalue method (Silver & Chan 1991) to find the splitting parameters ϕ'

and δt accrued along the ray. Pre- and post-analysis waveforms were manually inspected to check the quality of the result and find any null measurements. In some cases the waveforms are especially complicated and the splitting analysis cannot give a set of parameters which adequately linearises the particle motion, and in this case the result is noted but not used in the further analysis.

3 RESULTS AND DISCUSSION

3.1 Shear wave splitting predictions

Fig. 3 and the supporting information show the results for the nine paths considered and three plasticity cases, compared to the previous observations. The modelled splitting times are between 1.1 and 23.0 s, with the strongest variation between ray paths, and secondarily between plasticity models. Mean delay times, $\langle \delta t \rangle$, are largest for P100 (7.5 s) and smallest for P010 (3.2 s). This reflects the strength of the texture for the different models. For P010, individual slip system activities are more similar to each other, implying texture development should be weaker, and thus we might expect that this model should produce much smaller $\langle \delta t \rangle$ than the other models: this is not the case. One explanation may be that in regions of palaeo-subduction, the flow is dominantly downward (Figs 3, S1 and S2), hence texture has not had much time (pathline distance) to develop. The S1, W1 and Siberian paths cross the regions with the strongest textures (Figs S1 and S2), and here the values of δt are indeed much larger for the P001 case.

The waveforms produced are generally simple. The supporting information shows examples where clear elliptical particle motion results from applying the modelled splitting, and a clear minimum in the eigenvalue surface is evident. In two cases (path W1 for P100 and W2 for P001), the waveforms are too complicated to give a simple, single splitting operator which adequately recovers the initial, linear particle motion (supporting information). Therefore, these paths are rejected from further analysis.
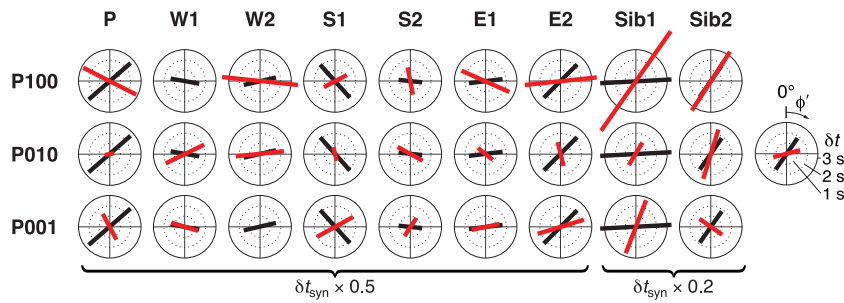
Figure 3. Shear wave splitting predicted by each plasticity model along each path (red), and observed splitting (black). Bars within circles show observed (black) and synthetic (red) splitting parameters. Orientation of bars represents fast orientation in ray frame, ϕ', and length shows delay time, δt, as for Fig. 1. Legend to right indicates where dotted inner circles show increasing δt, from 1 s to 3 s (circle edge). δt is scaled by 0.5 for all paths apart from Sib1 and Sib2 (where scaling is 0.2). W1 for P100 and W2 for P001 are excluded from analysis (see text).

3.2 Circular misfit

In order to quantitatively assess the fit of each of the plasticity models, and noting that a linear misfit is not appropriate for periodic data, we propose a 'circular misfit' in analogy to the reduced χ^2 misfit:

$$\chi_c^2 = \frac{1}{\nu} \sum_i^N \frac{\sin^2(\phi_{i,\text{obs}} - \phi_{i,\text{syn}})}{\sin^2(\sigma_{i,\text{obs}})} , \tag{1}$$

where N is the number of data, $\nu = N - 1$ is the number of degrees of freedom, ϕ is the observed or synthetic fast orientation and σ is the uncertainty in the observed orientations. These are orientational rather than directional data, hence observed and synthetic angles of $-90°$ and $90°$, respectively should give a misfit of 0, as inspection of the form of χ_c^2 shows. Although the values of ϕ_{syn} are themselves somewhat uncertain, incorporating these into the measure is difficult as the range in σ_{syn} is very large (varying from $1.0°$ to $24.3°$, with mean $7.3°$).

The misfit intentionally does not include δt. This is because the texture in the models is unrealistically strong, hence none of the models can be reasonably compared to the observed δt. This strong texture may be for several reasons. Primarily we do not incorporate any effects to limit texture, such as recrystallization, into the VPSC calculation. Any method to scale the values would also be arbitrary, and the subsequent fit would be entirely due to this. Therefore we include only ϕ': tests show that ϕ' is approximately independent of the scaling of the strength of anisotropy in our models, down to 10 per cent of the maximum texturing.

Fig. 4 compares the misfit for the texture models. P010 appears to match the observations best, while the other two have similar χ_c^2. We may test whether the fit of any model is significant by comparison with the case of random ϕ'_{obs}. The means and standard deviations of χ_c^2 for 500 000 random sets of orientations are used to compute the 1σ and 2σ limits (Fig. 4), noting that not all paths are included for each model as discussed previously. This shows that, while none of the models vary significantly from the random case at the 2σ level, all cases are significant at the 1σ level, with P010 fitting better than random.

The χ_c^2 of shear wave splitting predicted from three tomographic models with radial anisotropy in D″ are also shown. It is important to note that inversions for radially-symmetric shear wave anisotropy in D″ are still somewhat uncertain and the three models may be affected by similar biases. None of the tomography models differs significantly from random, which suggests that, in the regions for which we compare with observations, there is a stronger correlation between our P010 model than the currently available anisotropic seismic tomography models. This is likely due to the constraint
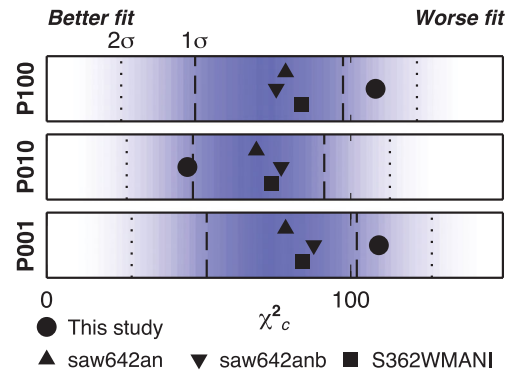
Figure 4. Misfit of synthetic shear wave splitting ϕ' compared to observations. The value of χ_c^2 for each model is shown by circles. Dashed and dotted lines show 1σ and 2σ bounds respectively of 500 000 sets of random ϕ'. The underlying shading shows histograms for the random χ_c^2 by colour intensity and are normalized to have the same maximum frequency. Values of χ_c^2 for three global anisotropic tomographic models are also shown, and vary between plasticity cases only because different paths are included in the calculation of χ_c^2 between the plasticity models: Panning & Romanowicz (2004) (saw642an; triangles); Panning *et al.* (2010) (saw642anb; inverted triangles); Kustowski *et al.* (2008) (S362WMANI; squares).

of radial anisotropy in the inversions, which allows only two values of ϕ': $0°$ and $90°$. The significant improvement offered by our models, by contrast, permits any orientation of ϕ', and allows the incorporation of more data than would otherwise be the case.

3.3 Discussion

Several causes of misfit between the predictions and observations are possible. First, ppv LPO may not be the cause everywhere, or at all, of D″ anisotropy in regions dominated by subducted material. However, we show that at present, the data do not require this to be the case. Secondly, the flow model we use may not accurately represent the true flow field. The TX2008 model is smooth, hence does not include any effects of strain localization such as strain-weakening rheologies (e.g. Yamazaki & Karato 2001), or weakening across the pv–ppv transition itself (e.g. Hunt *et al.* 2009). It also has no time dependence. Further, there is uncertainty in the viscosity profile, which may lead to different texturing, however previous work (Walker *et al.* 2011) suggests that the main effect of changing lower mantle viscosity in the the flow inversions is to scale the velocity of the flow, not the pattern, which would change only the delay times in this study. Thirdly, it is possible that none of the three plasticity models are an adequate description of

ppv's behaviour. For instance, point defect motion (Ammann *et al.* 2010), which would not necessarily generate LPO, is a potential mechanism which cannot at present be excluded. Finally, the ray-theoretical approach of the shear wave splitting modelling may not fully incorporate the effects of finite wave sensitivity to CMB structure. With current methods, forward modelling these observations at the correct frequency is computationally challenging, however we expect that doing so would not yield significantly different results, as the texture model varies very smoothly.

To within 1σ, our results suggest that one set of slip system activities in ppv predicts shear wave splitting in D″ better than random. At 2σ none of the models is significantly different, meaning we cannot rule out LPO in ppv as a cause of D″ anisotropy. The pattern of misfit—that one slip system matches observations while the other two do worse than random—is expected because of ppv's orthorhombic symmetry and the fact that the three plasticity models mainly favour slip on each of the three primary crystallographic planes. Our result is in agreement with previous work (Walker *et al.* 2011), where the approximation of hexagonal symmetry was imposed in the comparison with global *P*- and *S*-wave anisotropic tomography. With the global approach, the P100 and P010 cases could not be distinguished, whereas in this work we can conclude that slip on (010) in ppv LPO—or a mechanism related to flow, such as SPO of inclusions, which produces the same style of anisotropy—is most likely.

4 CONCLUSIONS

A new model of ppv texture in D″ imposing no constraints on the style of anisotropy predicts shear wave splitting in ScS waves which is compatible with observations in regions of palaeosubduction to within one standard deviation. Three different plasticity cases for dislocation creep in ppv are considered, with that favouring slip on (010) matching best. This corresponds to the mechanism predicted by previous computational and experimental work. Our approach means that as emerging data sets become available and mineral physical measurements improve, further data may be incorporated.

REFERENCES

Ammann, M.W., Brodholt, J.P., Wookey, J. & Dobson, D.P., 2010. First-principles constraints on diffusion in lower-mantle minerals and a weak D″ layer, *Nature,* **465,** 462–465.

Cordier, P., Amodeo, J. & Carrez, P., 2012. Modelling the rheology of MgO under Earth's mantle pressure, temperature and strain rates, *Nature,* **481,** 177–180.

Forte, A.M., 2000. Seismic-geodynamic constraints on mantle flow: implications for layered convection, mantle viscosity, and seismic anisotropy in the deep mantle, in *Earth's Deep Interior: Mineral Physics and Tomography from the Atomic to the Global Scale,* eds Karato, S., Forte, A.M., Liebermann, R.C., Masters, G. & Stixrude, L., *Geophys. Monogr. Ser.,* **117,** 3–36.

Forte, A.M. & Mitrovica, J.X., 2001. Deep-mantle high-viscosity flow and thermochemical structure inferred from seismic and geodynamic data, *Nature,* **410,** 1049–1056.

Hunt, S.A., Weidner, D.J., Li, L., Wang, L., Walte, N.P., Brodholt, J.P. & Dobson, D.P., 2009. Weakening of calcium iridate during its transformation from perovskite to post-perovskite, *Nat. Geosci.,* **2,** 794–797.

Iitaka, T., Hirose, K., Kawamura, K. & Murakami, M., 2004. The elasticity of the MgSiO₃ post-perovskite phase in the Earth's lowermost mantle, *Nature,* **430,** 442–445.

Kendall, J.-M. & Silver, P.G., 1996. Constraints from seismic anisotropy on the nature of the lowermost mantle, *Nature,* **381,** 409–412.

Kendall, J.-M. & Silver, P.G., 1998. Investigating causes of D″ anisotropy, in *The Core–Mantle Boundary Region,* pp. 97–118, eds Gurnis, M., Wysession, M.E., Knittle, E. & Buffett, B.A., *Geodynamic Series,* **28,** 97–118, American Geophysical Union, Washington, D.C., USA.

Kennett, B., Engdahl, E. & Buland, R., 1995. Constraints on seismic velocities in the Earth from travel-times, *Geophys. J. Int.,* **122,** 108–124.

Kustowski, B., Ekström, G. & Dziewoński, A., 2008. Anisotropic shear-wave velocity structure of the Earth's mantle: A global model, *J. Geophys. Res.,* **113**(B06306), doi:10.1029/2007JB005169.

Lay, T., Williams, Q., Garnero, E.J., Kellogg, L. & Wysession, M.E., 1998. Seismic wave anisotropy in the D″ region and its implications, in *The Core–Mantle Boundary Region,* pp. 299–318, eds Gurnis, M., Wysession, M.E., Knittle, E. & Buffett, B.A., American Geophysical Union, Washington, D.C., USA.

Lebensohn, R. & Tomé, C., 1993. A self-consistent anisotropic approach for the simulation of plastic-deformation and texture development of polycrystals—application to zirconium alloys, *Acta Metall. Mater.,* **41,** 2611–2624.

Lithgow-Bertelloni, C. & Richards, M., 1998. The dynamics of Cenozoic and Mesozoic plate motions, *Rev. Geophys.,* **36,** 27–78.

McCormack, R., Dobson, D.P., Walte, N.P., Miyajima, N., Taniguchi, T. & Wood, I.G., 2011. The development of shape- and crystallographic-preferred orientation in CaPtO₃ post-perovskite deformed in pure shear, *Am. Miner.,* **96,** 1630–1635.

McNamara, A.K., van Keken, P. & Karato, S., 2003. Development of finite strain in the convecting lower mantle and its implications for seismic anisotropy, *J. Geophys. Res.,* **108,** 2230, doi:10.1029/2002JB001970.

Merkel, S., McNamara, A.K., Kubo, A., Speziale, S., Miyagi, L., Meng, Y., Duffy, T.S. & Wenk, H.-R., 2007. Deformation of (Mg,Fe)SiO₃ post-perovskite and D″ anisotropy, *Science,* **316,** 1729–1732.

Metsue, A., Carrez, P., Mainprice, D. & Cordier, P., 2009. Numerical modelling of dislocations and deformation mechanisms in CaIrO₃ and MgGeO₃ post-perovskites—Comparison with MgSiO₃ post-perovskite, *Phys. Earth Planet. Inter.,* **174,** 165–173.

Mitrovica, J.X. & Forte, A.M., 2004. A new inference of mantle viscosity based upon joint inversion of convection and glacial isostatic adjustment data, *Earth Planet. Sci Lett,* **225,** 177–189.

Miyagi, L., Kanitpanyacharoen, W., Kaercher, P., Lee, K.K.M. & Wenk, H.-R., 2010. Slip systems in MgSiO₃ post-perovskite: Implications for D″ anisotropy, *Science,* **329,** 1639–1641.

Murakami, M., Hirose, K., Kawamura, K., Sata, N. & Ohishi, Y., 2004. Post-perovskite phase transition in MgSiO₃, *Science,* **304,** 855–858.

Niwa, K., Miyajima, N., Seto, Y., Ohgushi, K., Gotou, H. & Yagi, T., 2012. In situ observation of shear stress-induced perovskite to post-perovskite phase transition in CaIrO₃ and the development of its deformation texture in a diamond-anvil cell up to 30 GPa, *Phys. Earth Planet. Inter.,* **194-195,** 10–17.

Nowacki, A., Wookey, J. & Kendall, J.-M., 2010. Deformation of the lowermost mantle from seismic anisotropy, *Nature,* **467,** 1091–1095.

Nowacki, A., Wookey, J. & Kendall, J.-M., 2011. New advances in using seismic anisotropy, mineral physics and geodynamics to understand deformation in the lowermost mantle, *J. Geodyn.,* **52,** 205–228.

Nowacki, A., Kendall, J.-M. & Wookey, J., 2012. Mantle anisotropy beneath the Earth's mid-ocean ridges, *Earth Planet. Sci. Lett.,* **317-318,** 56–67.

Oganov, A. & Ono, S., 2004. Theoretical and experimental evidence for a post-perovskite phase of MgSiO₃ in Earth's D″ layer, *Nature,* **430,** 445–448.

Panning, M. & Romanowicz, B., 2004. Inferences on flow at the base of Earth's mantle based on seismic anisotropy, *Science,* **303,** 351–353.

Panning, M., Lekić, V. & Romanowicz, B., 2010. Importance of crustal corrections in the development of a new global model of radial anisotropy, *J. Geophys. Res.,* **115**(B12325), doi:10.1029/2010JB007520.

Ranganathan, S.I. & Ostoja-Starzewski, M., 2008. Universal elastic anisotropy index, *Phys. Rev. Lett.,* **101,** 055504, doi:10.1103/PhysRevLett.101.055504.

Shieh, S.R., Dorfman, S.M., Kubo, A., Prakapenka, V.B. & Duffy, T.S., 2011. Synthesis and equation of state of post-perovskites in the $(Mg,Fe)_3$ Al_2 Si_3 O_{12} system, *Earth Planet. Sci. Lett.,* **312,** 422–428.

Silver, P.G. & Chan, W.W., 1991. Shear-wave splitting and subcontinental mantle deformation, *J. Geophys. Res.,* **96,** 16429–16454.

Simmons, N.A., Forte, A.M. & Grand, S.P., 2009. Joint seismic, geodynamic and mineral physical constraints on three-dimensional mantle heterogeneity: implications for the relative importance of thermal versus compositional heterogeneity, *Geophys. J. Int.,* **177,** 1284–1304.

Simmons, N.A., Forte, A.M., Boschi, L. & Grand, S.P., 2010. GyPSuM: A joint tomographic model of mantle density and seismic wave speeds, *J. Geophys. Res.,* **115**(B12310), doi:10.1029/2010JB007631.

Stackhouse, S. & Brodholt, J.P., 2008. Elastic properties of the post-perovskite phase of Fe_2 O_3 and implications for ultra-low velocity zones, *Phys. Earth Planet. Inter.,* **170,** 260–266.

Stackhouse, S., Brodholt, J.P. & Price, G.D., 2006. Elastic anisotropy of $FeSiO_3$ end-members of the perovskite and post-perovskite phases, *Geophys. Res. Lett.,* **33**(L01304), doi:10.1029/2005GL023887.

Tsuchiya, T., Tsuchiya, J., Umemoto, K. & Wentzcovitch, R.M., 2004. Phase transition in $MgSiO_3$ perovskite in the earth's lower mantle, *Earth Planet. Sci. Lett.,* **224,** 241–248.

Walker, A.M., Forte, A.M., Wookey, J., Nowacki, A. & Kendall, J.-M., 2011. Elastic anisotropy of D″ predicted from global models of mantle flow, *Geochem. Geophys. Geosyst.,* **12**(Q10006), doi:10.1029/2011GC003732.

Wenk, H.-R., Speziale, S., McNamara, A.K. & Garnero, E.J., 2006. Modeling lower mantle anisotropy development in a subducting slab, *Earth Planet. Sci. Lett.,* **245,** 302–314.

Wenk, H.-R., Cottaar, S., Tomé, C.N., McNamara, A.K. & Romanowicz, B., 2011. Deformation in the lowermost mantle: From polycrystal plasticity to seismic anisotropy, *Earth Planet. Sci. Lett.,* **306,** 33–45.

Wentzcovitch, R.M., Tsuchiya, T. & Tsuchiya, J., 2006. $MgSiO_3$ postperovskite at D″ conditions, *Proc. Natl. Acad. Sci. USA,* **103,** 543–546.

Wookey, J. & Kendall, J.-M., 2008. Constraints on lowermost mantle mineralogy and fabric beneath Siberia from seismic anisotropy, *Earth Planet. Sci. Lett.,* **275,** 32–42.

Wookey, J., Kendall, J.-M. & Rümpker, G., 2005a. Lowermost mantle anisotropy beneath the north Pacific from differential S–ScS splitting, *Geophys. J. Int.,* **161,** 829–838.

Wookey, J., Stackhouse, S., Kendall, J.-M., Brodholt, J.P. & Price, G.D., 2005b. Efficacy of the post-perovskite phase as an explanation for lowermost-mantle seismic properties, *Nature,* **438,** 1004–1007.

Yamazaki, D. & Karato, S., 2001. Some mineral physics constraints on the rheology and geothermal structure of Earth's lower mantle, *Am. Miner.,* **86,** 385–391.

SUPPORTING INFORMATION

Additional Supporting Information may be found in the online version of this article:

Figure S1. Strength of anisotropy of elastic constants for each plasticity model used in the shear wave splitting calculations at radius 3555 km (75 km above the CMB). Shown are the values of A^U, the universal anisotropy index (Ranganathan & Ostoja-Starzewski 2008), for the aggregate elasticity tensors, evaluated each 5° in latitude and longitude. The three plasticity cases, P100, P010 and P001 are shown for the three regions investigated here (left: Northwest Pacific; middle: Americas; right: Siberia). Black squares show 5° blocks outside of the ppv stability field, hence no texturing is assumed. White area at top of Siberia plot show that no constants were evaluated outside the coloured area.

Figure S2. Strength of anisotropy of elastic constants for each plasticity model used in the shear wave splitting calculations at radius 3605 km (125 km above the CMB). Same as for Figure S1.

Figure S3. Strength of anisotropy of elastic constants for each plasticity model used in the shear wave splitting calculations at radius 3655 km (175 km above the CMB). Same as for Figure S1. Note that by comparison with the figure in the main text, and observing the instability region of ppv in NW Pacific, a double-crossing of the pv–ppv phase boundary has occurred in this region.

Figure S4. Examples of synthetic split waveforms and minimum eigenvalue surfaces. An example is given for each of the three plasticity models. Top panels show waveform before (left-hand side) and after (right-hand side) application of optimal apparent splitting operator when rotated to the optimal fast orientation. Middle panels show particle motion before and after correction with best splitting. Bottom panels show λ_2 surfaces for analysis, with the 95% confidence contour shown as thick line. Note W2 for P001 is excluded from further analysis because no single apparent splitting operator can recover adequately linear particle motion.

Figure S5. Strength of anisotropy for elastic constants without MgO (top), with MgO mixed with ppv (middle) and with MgO and ppv forming separated aggregates. Average and peak values of A^U are highest for the case without MgO, then for the mixture, then for the separated phase calculations.

Table S1. Event–receiver geometries for shear wave splitting measurements we compare to predictions from the texture model. Events and receivers are average (usually median) locations for average (NW Pacific) or stacked measurements of splitting.

Table S2. Synthetic shear wave splitting predicted from each plasticity model for each ray path. Paths W1 for P100 and W2 for the P001 model are excluded.

Table S3. Misfit of synthetic shear wave splitting fast orientations compared to previous observations for each plasticity model. (http://gji.oxfordjournals.org//lookup/supp1/doi:10.1093/gji/ggs068/-/DC1)

Please note: Oxford University Press is not responsible for the content or functionality of any supporting materials supplied by the authors. Any queries (other than missing material) should be directed to the corresponding author for the article.